



Cite this: *Phys. Chem. Chem. Phys.*,
2017, 19, 7807

DFT investigation of capacious, ultrafast and highly conductive hexagonal Cr₂C and V₂C monolayers as anode materials for high-performance lithium-ion batteries†

Zhenming Xu,^a Xiaojun Lv,*^a Jiangan Chen,^b Liangxing Jiang,^a Yanqing Lai^a and Jie Li^a

To assess the potential of hexagonal Cr₂C and V₂C monolayers as anode materials in lithium-ion batteries, first-principles calculations and AIMD simulations were carried out. AIMD simulations and phonon calculations revealed that the honeycomb structure of the hexagonal Cr₂C and V₂C monolayers is thermodynamically and dynamically stable. A single lithium atom is preferentially absorbed over the center of the honeycomb hollow. The full lithium storage phases of the hexagonal Cr₂C and V₂C monolayers correspond to Li₆Cr₂C and Li₆V₂C, with considerable theoretical specific capacities of 1386 and 1412 mA h g⁻¹, respectively. Interestingly, lithium ion diffusion on the hexagonal Cr₂C and V₂C monolayers is extremely fast, with low energy barriers of 32 and 28 meV, respectively; these values are much lower than those of other widely investigated anode materials. Moreover, the lithiated hexagonal Cr₂C and V₂C monolayers show enhanced metallic characteristics and excellent electronic conductivity during the entire lithiation process; these values are superior to those of other anode materials with semiconducting characteristics. The findings in our study suggest that hexagonal Cr₂C and V₂C monolayers are promising anode materials with high capacities and high rate capabilities for next generation high-performance lithium-ion batteries.

Received 4th January 2017,
Accepted 22nd February 2017

DOI: 10.1039/c7cp00064b

rsc.li/pccp

1. Introduction

The mature commercial technology of rechargeable lithium-ion batteries (LIBs) has been widely applied in portable electronic devices due to their outstanding reversible capacity, power density, and cycle life.^{1–5} However, current commercial LIB technologies are unsatisfactory to address the rapid demands of large-scale energy storage equipment such as electric vehicles and power backup systems.⁶ In a LIB system, the electrode materials play key roles and determine the electrochemical performance of the LIB.⁷ Although rapid progress is being made in research for new cathode materials, commercial anode materials for LIBs are limited to graphite due to its relatively good cycling stability and low-cost.^{8,9} Moreover, the relatively low capacity (372 mA h g⁻¹) and poor rate capability of graphite restrict its further applications in large-scale energy storage equipment.¹⁰ Accordingly, breakthroughs in enhanced electrode materials for next generation LIBs to meet large-scale energy

storage demands are urgently required. Researchers are continually searching for new energetic materials with high capacities and high ion diffusion to meet the requirements of next generation LIBs and sodium-ion batteries (SIBs). Many two-dimensional (2D) materials including graphene/MoS₂,^{11–13} graphyne,^{14–16} phosphorene,^{17–19} transition-metal dichalcogenides,^{20–24} and MXenes,^{25,26} which have flat surfaces, high surface areas and plentiful adsorption sites, have been identified as promising anode materials for LIBs and SIBs due to their high energy densities and high rate capabilities. Among these, MXenes, 2D transition metal carbides (TMCs) with metallic conductivity, exhibit desirable properties as electrode materials for LIBs and SIBs. M. Naguib *et al.* reported Ti₂C sheets exhibiting a stable capacity of 225 mA h g⁻¹ at a C/25 rate.²⁷ New two-dimensional Nb₂AlC and V₂AlC materials, synthesized by selective etching, demonstrate reversible capacities of 170 and 260 mA h g⁻¹ at 1C, and 110 and 125 mA h g⁻¹ at 10C, respectively.²⁸ Meanwhile, theoretical calculations for trigonal phase MXenes exhibiting superconductivity have made some progress. The theoretical lithium storage capacities and excellent lithium diffusion abilities of 1T-Ti₂C,²⁹ Ti₃C₂,^{30,31} 1T-V₂C,³² 1T-Cr₂C^{33,34} and 1H-Mo₂C monolayer¹⁰ have been revealed by density functional theory (DFT).

^a School of Metallurgy and Environment, Central South University, No. 932, Lushan South Road, Changsha 410083, China. E-mail: bxiaojun@csu.edu.cn

^b Faculty of Resource and Environmental Engineering, Jiangxi University of Science and Technology, No. 86, Hongqi Road, Ganzhou 341000, China

† Electronic supplementary information (ESI) available. See DOI: 10.1039/c7cp00064b

Inspired by the excellent performance of the previously reported 1T phase Cr₂C and V₂C monolayers as anode materials for LIBs, we pondered three main questions: are 1H-Cr₂C and V₂C monolayers thermodynamically and dynamically stable? Can the hexagonal phase MXenes of 1H-Cr₂C and V₂C monolayers be applied as anodes for LIBs? Are the lithium storage and migration capabilities of the hexagonal phase Cr₂C and V₂C monolayers better than those of the corresponding 1T phases? To the best of our knowledge, to date, very little experimental effort or research regarding lithium storage on 1H-Cr₂C and V₂C monolayers has been reported, even for theoretical calculations. To answer these three questions, detailed studies of the electronic and lithium storage properties of the proposed 1H-Cr₂C and V₂C monolayers are urgently needed to identify suitable electrodes for rechargeable batteries.

To evaluate their potential and advantages as anode materials in LIBs, herein, first-principles calculations based on density functional theory (DFT) were performed for the first time to study the energetics and dynamics of lithium atoms on the proposed 1H-Cr₂C and V₂C monolayers. The structures of the 1H-Cr₂C and V₂C monolayers were firstly optimized; then, their electronic structures were calculated to examine their excellent electron conductivities. Calculations of phonon spectra and *ab initio* molecular dynamics (AIMD) simulations were performed to verify the thermal and dynamical stabilities of the materials. Subsequently, the adsorption energies and Hirshfeld charges of lithium on the possible high-symmetry adsorption sites of the 1H-Cr₂C and V₂C monolayers were studied. In order to determine the maximum theoretical lithium storage capacities, the most stable structures of the lithiated 1H-Cr₂C and V₂C monolayers with increasing lithium concentration were investigated. Using the linear synchronous transit/quadratic synchronous transit (LST/QST) method, the migration processes of lithium ions on the 1H-Cr₂C and V₂C monolayers were probed. Finally, the electronic conductivities of the lithiated 1H-Cr₂C and V₂C monolayers were further investigated by calculating their electron densities of states (DOS).

2. Computational methods

In this work, all calculations were performed using the Cambridge Sequential Total Energy Package (CASTEP) based on density functional theory (DFT). The Perdew–Burke–Ernzerhof (PBE)³⁵ exchange function of the generalized gradient approximation (GGA) was chosen for the calculations, and the ultrasoft pseudopotentials (USPPs) introduced by Vanderbilt³⁶ were employed for all the ion–electron interactions. Herein, Li 1s²2s¹, V 3s²3p⁶3d³4s², Cr 3s²3p⁶3d⁵4s¹, and C 2s²2p² electrons were explicitly regarded as valence electrons. The convergences with respect to both energy cutoff and *k*-point mesh were strictly tested. Considering both the convergence tests and the computational efficiency, an energy cutoff of 500 eV was chosen for the 1H-Cr₂C and V₂C monolayers to ensure that the total energies were converged within 1×10^{-4} eV per atom, respectively. For geometry optimization and energy calculations, Brillouin zone sampling of

the 1H-Cr₂C and V₂C monolayer units was carried out with $16 \times 16 \times 1$ meshes using the Monkhorst–Pack method.³⁷ Meanwhile, for the density of states (DOS) calculations, the double mesh of $32 \times 32 \times 1$ was used for the 1H-Cr₂C and V₂C monolayer units. For all subsequent supercell calculations, *k*-point meshes with the same density as the unit cell were used. The energy convergence criterion for the self-consistent field (SCF) calculation was set to 1×10^{-6} eV per atom. To more accurately describe the electronic structures, the spin-dependent GGA plus Hubbard *U* (GGA+*U*) method was employed, along with strong onsite Coulomb repulsion between the localized transition metal 3d electrons of chromium and vanadium elements. Herein, the *U* values of Cr and V atoms were set as 12 and 4.5 eV, respectively.³⁸

In order to locate the most stable configurations of pristine 1H-Cr₂C and V₂C monolayers and lithiated 1H-Cr₂C and V₂C monolayers, atom and cell optimizations were performed beforehand using total energy minimization methods. The total energy difference was within 10^{-6} eV per atom, the maximum force was within 10^{-4} eV Å⁻¹, the maximum stress was within 0.01 GPa and the maximum atom displacement was within 10⁻⁴ Å. Two-dimensional periodic boundary conditions were introduced to all the calculations for the pristine and lithiated 1H-Cr₂C and V₂C monolayers. Moreover, to simulate the monolayers and eliminate the interactions between adjacent conformations, a vacuum region of 15 Å was applied in the direction perpendicular to the pristine and lithiated 1H-Cr₂C and V₂C monolayer planes. For phonon calculations, the non-conserving pseudopotentials and linear response methods were used; therefore, the corresponding cutoff energy was increased to 800 eV. Additionally, AIMD simulations were carried out with a 4×4 supercell for the 1H-Cr₂C and V₂C monolayers at room temperature (300 K) using a statistical ensemble with fixed particle number, volume and temperature (*NVT*). The time step was set to 2 fs, and the supercell systems were equilibrated for 10 ps. An energy cutoff of 350 eV, a Gamma *k*-point mesh and periodic boundary conditions were employed during the AIMD simulations for the 4×4 supercell systems.

3. Results and discussion

3.1 Stabilities and electronic structures of hexagonal Cr₂C and V₂C monolayers

Firstly, the structures of the hexagonal Cr₂C and V₂C monolayers were relaxed, as depicted in Fig. 1a and b. The lattice structure of the Cr₂C and V₂C monolayers belongs to the hexagonal crystal system; the monolayers were named 1H-Cr₂C and 1H-V₂C. Analogous to the common transitional-metal dichalcogenides (TMDs), which include MoS₂, WS₂, and MoSe₂, each 1H-Cr₂C or V₂C monolayer is composed of a triple layer (sandwich structure), where atoms are stacked in a sequence of Cr(V)–C–Cr(V) with atomic thicknesses of 2.548 and 2.556 Å, respectively. The optimized lattice parameters for the 1H-Cr₂C and V₂C monolayers are found to be $a = b = 2.659$ and 2.775 Å, and the bond lengths of Cr–C and V–C are 1.975 and 2.049 Å in the ground state, respectively.

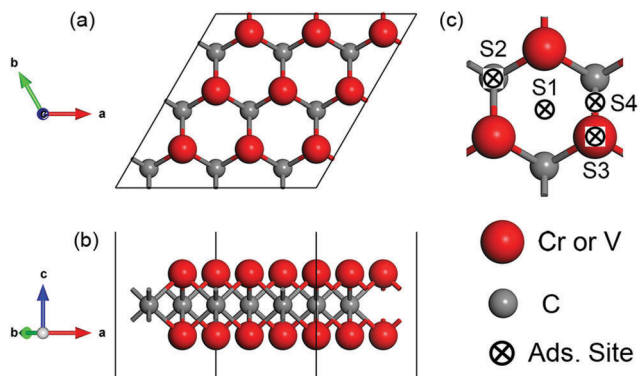


Fig. 1 Optimized geometry (3×3 supercell) of the 1H-Cr₂C and V₂C monolayers: (a) top view; (b) side view. (c) Four possible lithium adsorption sites on the surfaces of the 1H-Cr₂C and V₂C monolayers.

To date, no experimental report of the synthesis of 2D ultrathin 1H-Cr₂C and V₂C has been published; therefore, we proposed that verifying the thermal and dynamical stability of 1H-Cr₂C and V₂C should be the top priority before carrying out the subsequent lithium storage and diffusion calculations on the 1H-Cr₂C and V₂C monolayers. Starting from here, AIMD simulations at a room temperature of 300 K were carried out to examine the thermal stabilities of the 1H-Cr₂C and V₂C monolayers. During the entire AIMD process of 5000 steps (10 ps) at 300 K, no broken Cr-C and V-C bonds or obvious geometric reconstructions of the 1H-Cr₂C and V₂C monolayers were observed, as demonstrated in the movie provided in the supporting videos (ESI[†]). As depicted in Fig. 2a and b, the snapshot of the geometrical structures of the 1H-Cr₂C and V₂C monolayers extracted from AIMD simulations at 300 K shows the most significant distortion in the blue circles, with sustainable movement of the Cr and V atoms, in the upper and lower atomic layers; this indicates that the entire honeycomb structures of the 1H-Cr₂C and V₂C monolayers are stable at 300 K. Compared to the 1H-V₂C monolayer, the 1H-Cr₂C monolayer is more thermodynamically stable due to the minor distortion of its Cr atom (Fig. 2a and b), its lower range of potential energy (Fig. 2c and d) and the smaller mean square of displacement for Cr and C atoms in the 1H-Cr₂C monolayer. Furthermore, AIMD simulations of the 1H-Cr₂C and V₂C monolayers at high temperature (from 800 to 1300 K) were carried out. AIMD shows that the amplitude of thermal vibration increases significantly with increasing temperature. For the 1H-Cr₂C and V₂C monolayers, the highest temperatures where the honeycomb structure can be maintained without serious distortion are 850 and 1250 K, respectively (see supporting videos, ESI[†]). Therefore, we can conclude that the thermal stability of the 1H-Cr₂C monolayer is superior to that of the 1H-V₂C monolayer.

On the other hand, atoms in solid materials are constantly vibrating at very high frequencies and with relatively small amplitudes. The vibrational thermal energies for a material have a range of distributions and frequencies and are said to be quantized. A single quantum of vibrational energy is called a phonon (a phonon is analogous to the quantum of electromagnetic

radiation, the photon). Their frequencies (ω) reflect the stiffness of the bonds in the material. An imaginary frequency (negative second derivative of the energy) precisely represents the instability of the material. If all frequencies meet the condition of $\omega > 0$, the corresponding structure is locally stable with a minimum energy. Therefore, the phonon dispersion curves are effective for evaluating structural stability. Fig. 2c and d show the phonon dispersion curves as a function of frequency for the 1H-Cr₂C and V₂C monolayers, respectively; here, negative frequencies were used to represent the imaginary values.

There are three atoms in a unit cell of Cr(V)₂C; thus, there are nine corresponding phonon branches (three acoustic and six optical modes). According to their symmetries and frequencies at the Γ point, the three acoustic modes are divided into the in-plane transverse and longitudinal acoustic modes, named the TA and LA modes, respectively, and the out-of-plane transverse acoustic mode, named the ZA mode. The six optical modes are labeled as the TO, LO, ZO, TO*, LO* and ZO* modes. The TO and LO (TO* and LO*) modes correspond to the in-plane transverse and longitudinal symmetric (antisymmetric) optical modes. The ZO (ZO*) mode represents the out-of-plane transverse symmetric (antisymmetric) optical mode with the two Cr(V) atoms in the same (reverse) vibration direction. The anion C atom is symmetrically sandwiched by the cation of the Cr(V) atom to conserve the mass center; therefore, the antisymmetric TO*, LO*, and ZO* modes can be regarded as the vibrations of Cr(V) atoms. In contrast to ionic polarization crystal materials, there is no LO-TO splitting near the Γ point, which embodies the metallic character of the 1H-Cr(V)₂C monolayer. This lack of LO-TO splitting is ubiquitous in two-dimensional systems and has been reported in some published studies regarding single-layer MXenes and dichalcogenides.^{39,40}

Near the Γ point, the TA and LA modes are conventionally linear, and their slopes correspond to their group velocities. Meanwhile, the out-of-plane transverse ZA mode demonstrates a parabolic dispersion near the Γ point; this ZA mode is a ubiquitous phenomenon in 2D systems. Far from the Γ point, the symmetry of phonon dispersions changes because the nonorthogonal Cr(V)-C bonds (referring to both the XY plane and Z direction) arouse hybrid vibrations in the XY plane and in the Z direction. However, there are many differences between Cr₂C and V₂C. For the ZA branches, the frequencies of V₂C are lower than those of Cr₂C, indicating that the flexural movements of the V₂C monolayer out of plane are stronger than those of the Cr₂C monolayer. For the antisymmetric optical branches, the two ZO* modes do not differ greatly. Meanwhile, the TO* and LO* modes of V₂C are lower than those of Cr₂C. In other words, Cr(V) atoms show remarkably different vibration behaviors in the planes of the Cr₂C and V₂C monolayers. Among the symmetric optical modes of the contributions of the Cr(V) and C atoms, the ZO modes dominate the highest frequencies of the Cr₂C monolayer, while the TO modes dominate the highest frequencies of the V₂C monolayer. This may be caused by the differences in the masses of the transition metals and the binding strengths of the Cr(V)-C bonds; these differences are also found between Mo₂C and Mo₂N monolayers.³⁹ All the information

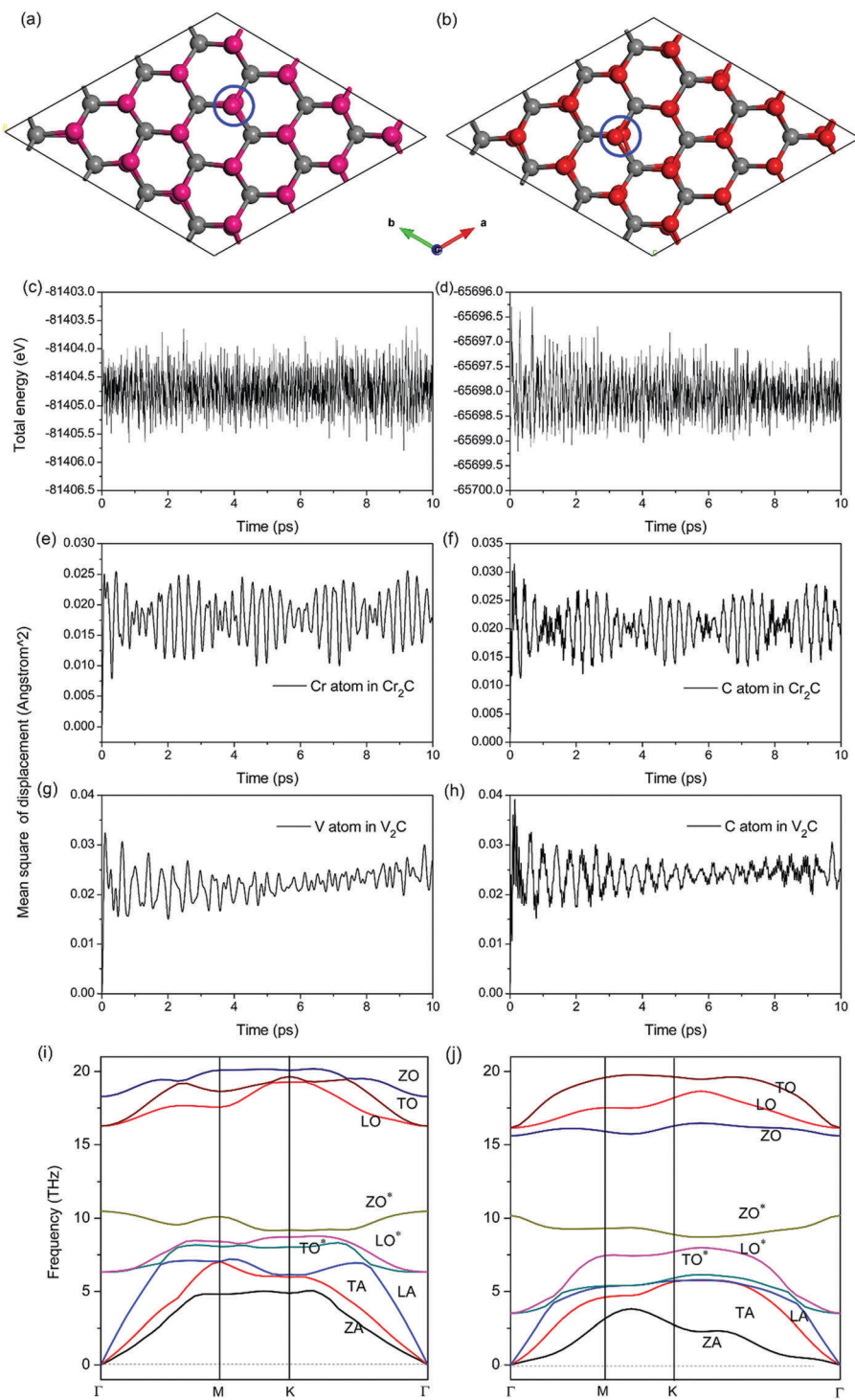


Fig. 2 Snapshots of (a) 1H-Cr₂C and (b) 1H-V₂C monolayer structures with the largest atomic distortions extracted from AIMD simulations at a temperature of 300 K; the local enlargements of the maximum geometric distortions for the Cr and V atoms are indicated by the blue circles. Potential energies of (c) 1H-Cr₂C and (d) 1H-V₂C monolayer systems during the entire AIMD simulations with a time scale of 10 ps. The mean squares of displacement for (e) Cr atom and (f) C atom of the 1H-Cr₂C monolayer and (g) V atom and (h) C atom of the 1H-V₂C monolayer during the 10 ps AIMD simulations. Calculated phonon dispersion curves as a function of frequency for the (i) 1H-Cr₂C and (j) 1H-V₂C monolayers.

from the phonon dispersions indicates that the thermal vibration of the 1H-Cr₂C monolayer is lower than that of the 1H-V₂C monolayer, which is also in good agreement with the AIMD results.

Because all the ω values of the predicted 1H-Cr₂C and V₂C monolayer materials exhibit positive frequencies, it is expected that the 1H-Cr₂C and V₂C monolayers are locally stable or at least structurally metastable. Consequently, based on the

present analysis of AIMD simulations and phonon dispersion curves, the honeycomb structures of the 1H-Cr₂C and V₂C monolayers are thermodynamically and dynamically stable in general. Thus, we confidently proceeded with the subsequent studies of lithium storage and diffusion on the 1H-Cr₂C and V₂C monolayers.

Electronic conductivity is a critical factor in determining the rate capability performance of electrode materials. Using the optimized structures, the intrinsic electronic structures of the 1H-Cr₂C and V₂C monolayers were calculated, including the band structures and spin-polarized partial densities of states (PDOS), as depicted in Fig. 3. As can be seen from the band structures in Fig. 3a and b, the substantial electron states crossing the Fermi levels indicate that the 1H-Cr₂C and V₂C monolayers demonstrate metallic behavior, corresponding to other MXenes (*e.g.* 1H-Mo₂C,¹⁰ 1T-Cr₂C³³ and 1T-V₂C³⁴). As can be seen from the PDOS results plotted in Fig. 3d and f, at first glance, the DOS near the Fermi level for both the 1H-Cr₂C and V₂C monolayer systems are dominated by the Cr-3d and V-3d orbitals, respectively. Furthermore, it is worth noting that the spin-up and spin-down DOS for the V-3d orbital of the 1H-V₂C monolayer are misaligned, which simply reflects the ferromagnetic phase structure with a net magnetic moment of

1.8 μ_B per 1H-V₂C cell unit. Meanwhile, the spin-up and spin-down DOS for the Cr-3d orbital of the 1H-Cr₂C monolayer basically coincide with each other, with an insignificant net magnetic moment of 0.1 μ_B per cell unit. Therefore, the 1H-Cr₂C monolayer shows nonmagnetic characteristics, which is different from the obvious ferromagnetic behavior of 1T-Cr₂C.³³ It is worth noting that the electronic structures calculated by DFT are based on 0 K and may change slightly at room temperature. However, the qualitative conductivity properties of the metallic characteristics of the 1H-Cr₂C and V₂C monolayers would not change, exhibiting small charge transfer resistance and good electronic conduction. This outstanding feature represents the greatest advantage of the 1H-Cr₂C and V₂C monolayers and is very important for their applications as battery electrodes.

3.2 Li adsorption on hexagonal Cr₂C and V₂C monolayers

A fundamental requirement of a promising anode material for LIBs is that the material must have a relatively high specific capacity, especially for high power density applications such as electric vehicles. It is known that the specific capacity is mainly dependent on the large lithium storage. The adsorption energy of lithium on the layer determines the specific capacity of the 1H-Cr₂C and V₂C monolayer materials. To locate the most

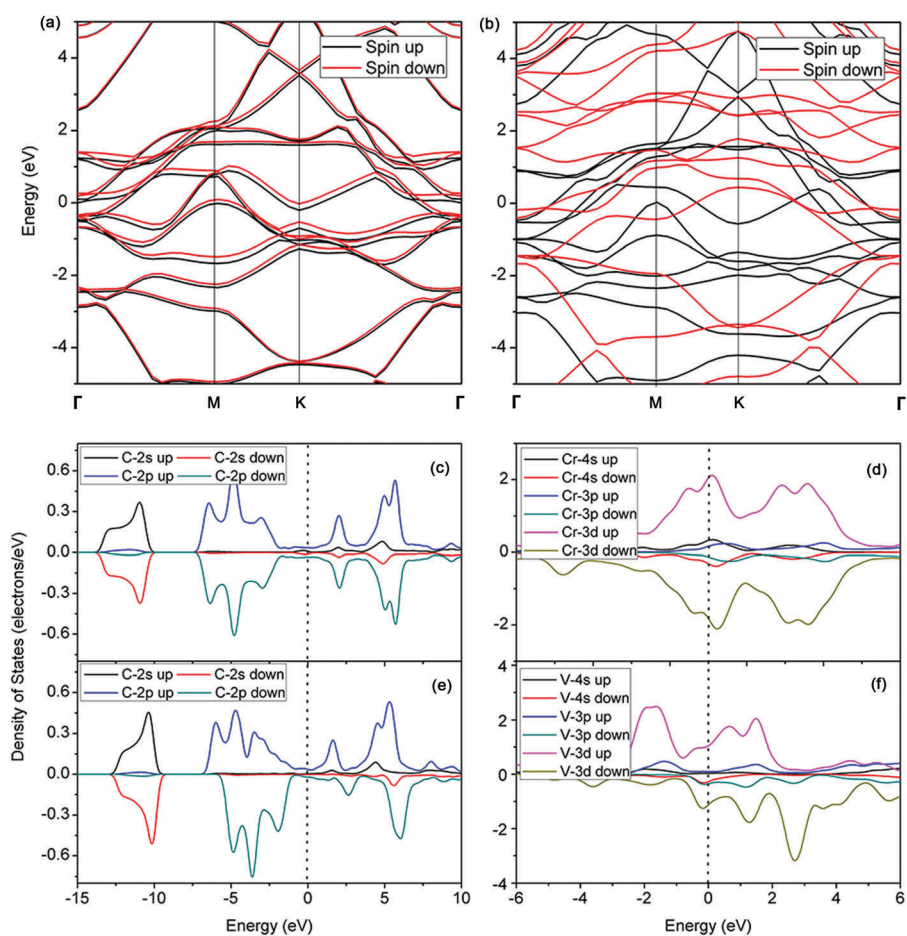


Fig. 3 Band structures of the (a) 1H-Cr₂C and (b) 1H-V₂C monolayers; spin-polarized partial densities of states (PDOS) of C atom in the (c) 1H-Cr₂C and (d) 1H-V₂C monolayers; PDOS of Cr and V atoms in the (e) 1H-Cr₂C and (f) 1H-V₂C monolayers. The Fermi levels are set to zero.

stable adsorption sites of the 1H-Cr₂C and V₂C monolayers, the adsorption behaviors of a single lithium atom on the four possible high-symmetry adsorption sites of the 2 × 2 1H-Cr₂C and V₂C monolayers were firstly examined, as plotted in Fig. 1c: (a) S1 site: over the center of the hexagonal atom hollow; (b) S2 site: the top of a C atom; (c) S3 site: the top of a Cr(V) atom; and (d) S4 site: over the center of the Cr(V)-C bond. It is worth noting that according to previous studies, the supercell size would not change the order of the calculated adsorption energy for a single atom;^{41,42} therefore, the 2 × 2 supercell was used in this work to increase the speed of calculation. The stability of the lithiated 1H-Cr₂C and V₂C monolayer systems can be estimated by their corresponding single lithium adsorption energies (E_a). The adsorption energy can be calculated by the following equation:^{43,44}

$$E_a = [E(\text{Li-Cr}_2\text{C or V}_2\text{C monolayer}) - E(\text{Cr}_2\text{C or V}_2\text{C monolayer}) - E(\text{Li})] \quad (1)$$

where $E(\text{Li-Cr}_2\text{C or V}_2\text{C monolayer})$, $E(\text{Cr}_2\text{C or V}_2\text{C monolayer})$ and $E(\text{Li})$ are the total energy of the lithiated Cr₂C or V₂C monolayer system, the pure 1H-Cr₂C or V₂C monolayer and a lithium atom in its bulk phase, respectively.

Full geometry optimizations for the structures of the lithiated 1H-Cr₂C and V₂C monolayers were performed. The calculated adsorption energies (E_{ads}), adsorption heights and Hirshfeld charges of a single lithium atom adsorbed on a 2 × 2 1H-Cr₂C or V₂C monolayer are listed in Table 1. For both the 1H-Cr₂C and V₂C monolayers, the S1 site over the center of the hexagonal atom hollow was found to be the most stable, with the highest adsorption energies of −0.463 and −0.451 eV, respectively. Therefore, the adsorption of lithium atoms on the S1 sites of the 1H-Cr₂C and V₂C monolayer surfaces is free of clusters, which is beneficial to safety during the charging and discharging process of LIBs. In the case of S1 site adsorption, the adsorption heights of the distance between the lithium atom and the planes of the 1H-Cr₂C and V₂C monolayers are the smallest (2.256 and 2.363 Å, respectively). More interestingly, the adsorption energies, adsorption heights and Hirshfeld charges of lithium adsorption on the S4 sites are fully equal to those of the S2 sites because the lithium ion can move from the S4 site to the S2 site without needing to cross the energy barrier after optimization.

Table 1 Adsorption energies (E_{ads} in eV), adsorption heights (in Å) and Hirshfeld charges (in e) of a single lithium atom adsorbed on 2 × 2 1H-Cr₂C and V₂C monolayers

Monolayer	Adsorption site	E_{ads}	Adsorption height	Hirshfeld charge
1H-Cr ₂ C	S1	−0.463	2.256	0.21
	S2	−0.437	3.531	0.22
	S3	−0.380	2.390	0.22
	S4	−0.437	3.531	0.22
1H-V ₂ C	S1	−0.451	2.363	0.25
	S2	−0.418	3.651	0.26
	S3	−0.352	2.506	0.25
	S4	−0.418	3.651	0.26

Meanwhile, lithium adsorption on the S3 sites of the 1H-Cr₂C and V₂C monolayers demonstrates the lowest adsorption energies of −0.380 and −0.352 eV, respectively. The negative adsorption energies for all adsorption sites on the 1H-Cr₂C and V₂C monolayer surfaces reveal that Li storage on these monolayers is exothermic and spontaneous. This feature is necessary and beneficial for Li-ion battery applications. Comparing the 1H-Cr₂C and V₂C monolayers, it is found that the strength of adsorption of one lithium atom on the 1H-Cr₂C monolayer is larger than that on the 1H-V₂C monolayer due to the larger adsorption energy and adsorption height. However, in the case of the 1H-Cr₂C monolayer, the amount of charge transfer (0.22 e) from the lithium atom to the adsorption substrate is slightly less than that of the 1H-V₂C monolayer (0.26 e), demonstrating that the decisive factor of the adsorption strength is not the charge transfer alone and that the size of the atom may be another important factor. The difference in the adsorption energies between different adsorption sites varies significantly, indicating that lithium migrates between adjacent adsorption sites by leap rather than flow.

To gain further insight into the differences in the adsorption sites and the mechanism of the multilayer lithium adsorption behavior, the electrostatic potentials of the (110) sections for the 1H-Cr₂C and V₂C monolayers were determined and are plotted in Fig. 4. As can be seen from Fig. 4a and b, all the electronic states are localized to form ionic bonds; electron hollows (areas without electrons) are also observed. Moreover, it can be clearly seen that the S1 and S3 sites of the 1H-Cr₂C and V₂C monolayers are all located in the potential valleys, where the negative electrostatic potential is lowest. Therefore, the electropositive Li ions preferentially reside in the potential valleys (electron hollows), corresponding to the strongest lithium adsorption.

3.3 Theoretical specific capacities of lithium storage on hexagonal Cr₂C and V₂C monolayers

To explore the theoretical maximum capacities of lithium storage on the 1H-Cr₂C and V₂C monolayers, the lithium adsorptions on (2 × 2) 1H-Cr₂C and V₂C monolayers were investigated by loading the lithium multilayers on both sides. In other words, the extra lithium ions store on the 2 × 2 supercell of 1H-Cr₂C and V₂C surface layer by layer. Here, we examined the half-cell reaction involving the charge–discharge processes:³² Cr(V)₂C + xLi⁺ + xe[−] ↔ Li_xCr(V)₂C. On charging, the electrons flow onto

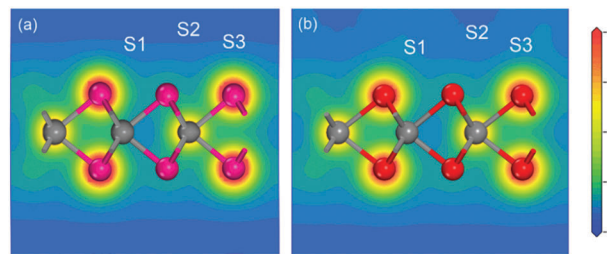


Fig. 4 Electrostatic potentials (in eV) of the (110) section for the (a) 1H-Cr₂C and (b) 1H-V₂C monolayers.

the anode, and Li ions are removed or deintercalated from the cathode compound and intercalated onto the Cr(V)₂C monolayer. The average adsorption energy is defined as the difference in the total energy of the 1H-Cr₂C or V₂C monolayer before and after lithium ion intercalation. In this work, the changes in volume and entropy during lithium extraction and insertion are accordingly negligible. For lithium intercalation on the 1H-Cr₂C and V₂C monolayers, the first layer of lithium is adsorbed on the favorable S1 sites above the center of the honeycomb lattice, named Li₂Cr(V)₂C. After the favorable S1 adsorption sites in the first layer are completely occupied, the subsequently added lithium will reside on the S2 sites above the C atoms, forming the second lithium layer, named Li₄Cr(V)₂C-I. Moreover, in the case of two lithium adsorption layers, the reversed adsorption sequence was also considered due to the small difference in the adsorption energies of the S1 and S2 sites, in which the first and second lithium layers are based on the S2 and S1 sites, respectively, named Li₄Cr(V)₂C-II. When all the S1 and S2 adsorption sites in the first and second layers are completely occupied, additional lithium will form the third adsorbed layer above the previous lithium ions adsorbed on the S2 sites in the second layer, named Li₆Cr(V)₂C. The fourth lithium layer was not considered in this work because lithium ions in this layer are distant from the surface of the 1H-Cr₂C and V₂C monolayers and are not involved in charge transfer. To assess the bonding strengths between the lithium layers and the host 1H-Cr₂C and V₂C monolayer materials, the average adsorption energies for each lithium layer (E_a) were calculated according to the following

equation: $E_a = 1/8[E(\text{Li}_{8n}\text{Cr}(\text{V})_2\text{C}) - E(\text{Li}_{8(n-1)}\text{Cr}(\text{V})_2\text{C}) - 8E(\text{Li})]$. Here, $E(\text{Li})$ denotes the energy of one Li atom, referring to the Li metal bulk, and $E(\text{Li}_{8n}\text{Cr}(\text{V})_2\text{C})$ and $E(\text{Li}_{8(n-1)}\text{Cr}(\text{V})_2\text{C})$ represent the total energy of 1H-Cr₂C or V₂C with n and $(n-1)$ adsorbed lithium layers, respectively. The number “8” in this formula denotes a total of eight lithium adsorption sites in each layer for a 2×2 supercell (two sides) (Fig. 5).

The calculated average adsorption energies of the lithium layers on the 1H-Cr₂C and V₂C monolayers are listed in Table 2. It is found that all the adsorption energies referring to the Li bulk phase are negative, indicating that the lithium storage on these monolayers is exothermic and spontaneous. This outstanding structural stability is highly significant for the process of lithiation/delithiation. As the number of lithium layers increases, the adsorption energy gradually decreases, which indicates a reduction of thermodynamic stability during the process of continuous adsorption of lithium. The decrease in the average adsorption energy may be due to the fact that the weak electrostatic attractions between the 1H-Cr₂C and V₂C monolayer hosts and lithium adatoms are gradually overcome by the enhanced Li-Li electrostatic repulsion at relatively high lithium concentrations.

To gain more insight into the mechanism of the multilayer lithium adsorption behavior, the charge density differences of the (110) section for the 1H-Cr₂C and V₂C monolayers were calculated and are plotted in Fig. 6. The results show that the inner Cr(V) and C atoms have ionic bond character due to the highly localized electrons around them. Making comparison

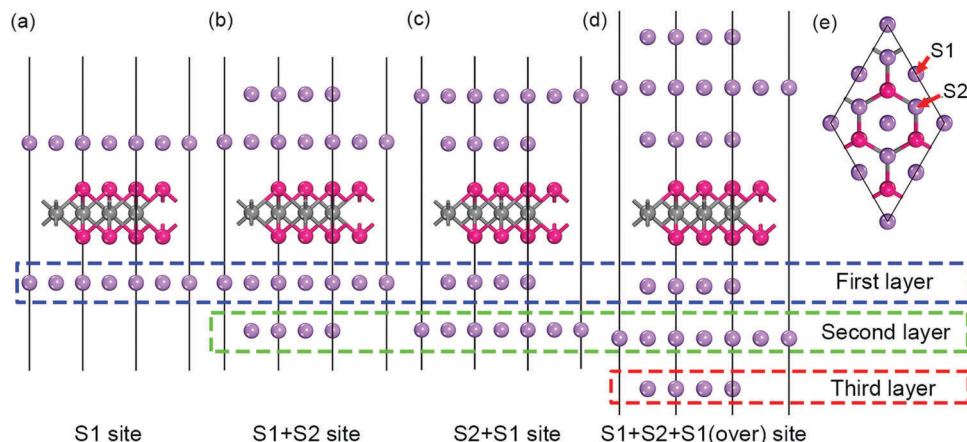


Fig. 5 Side and top views (e) of the structures of (a) Li₂Cr(V)₂C, (b) Li₄Cr(V)₂C-I, (c) Li₄Cr(V)₂C-II and (d) Li₆Cr(V)₂C with layers of lithium adsorbed on the S1 and S2 sites.

Table 2 Calculated average adsorption energies (in eV), theoretical specific capacities (mA h g⁻¹) and work functions (in eV) for lithium storage on the 1H-Cr₂C and V₂C monolayers with different adsorbed lithium layers

Species	Lithium layer	$E_a(\text{Cr}_2\text{C})$	Theoretical capacity (Cr ₂ C)	$E_a(\text{V}_2\text{C})$	Theoretical capacity (V ₂ C)	Work function	
						Cr ₂ C(4.8)	V ₂ C(4.144)
Li ₂ Cr(V) ₂ C	1	-0.292	462	-0.831	471	3.807	3.671
Li ₄ Cr(V) ₂ C-I	2	-0.264	924	-0.764	940	3.565	3.468
Li ₄ Cr(V) ₂ C-II	2	-0.260	924	-0.661	940	3.763	3.485
Li ₆ Cr(V) ₂ C	3	-0.198	1386	-0.579	1412	3.135	3.013

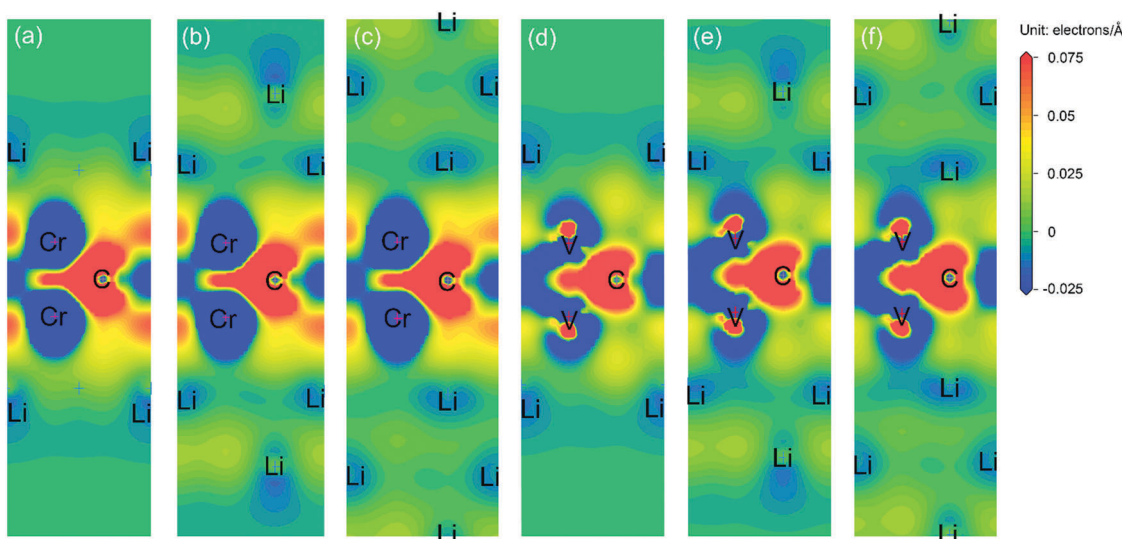


Fig. 6 Charge density differences of the (110) section for the (a–c) 1H- Cr_2C and (d–f) 1H- V_2C monolayers with one, two and three layers of lithium atoms. The red area represents charge aggregation, and the blue area represents charge depletion.

among these 1H- Cr_2C and V_2C monolayers with one, two and three layers of lithium atoms, we find that numerous electrons are spread out in the outer lithium layers like free negative electron gases, as in metals.^{31,45,46} Therefore, we can conclude that numerous electrons are transferred from the inner lithium layer to the outer layer. These dispersive electron clouds among the outer lithium atoms may stabilize the lithium adsorption due to the screen effect among these positive Li ions near the surface;⁴⁵ they may also play the role of negative electron glues attracting the positive Li ion layers. This is a special advantage of the 1H- Cr_2C and V_2C monolayers as electrode materials in lithium-ion batteries.

The full lithium storage phases of the 1H- Cr_2C and V_2C monolayers should meet the following four conditions: (a) the lithium concentration is maximal; (b) the average lithium adsorption energy referring to the Li bulk phase is less than zero; (c) no lithium atoms extrude from the 1H- Cr_2C and V_2C monolayers; (d) no irreversible deformation of the structures of the 1H- Cr_2C and V_2C monolayers occurs.^{18,47} By examining all the optimized structures and their corresponding adsorption energies, the maximum layer number of lithium adsorption on the 2×2 1H- Cr_2C and V_2C monolayer surfaces is $n = 3$, corresponding to the chemical stoichiometry of $\text{Li}_6\text{Cr}_2\text{C}$ and $\text{Li}_6\text{V}_2\text{C}$, respectively, as listed in Table 2. The lithium adsorption energies of the $\text{Li}_6\text{Cr}_2\text{C}$ and $\text{Li}_6\text{V}_2\text{C}$ systems are -0.198 and -0.579 eV per Li atom, respectively; thus, the lithium atoms are free of clusters, which is beneficial to safety during the process of lithiation. For $\text{Li}_4\text{Cr}(\text{V})_2\text{C-I}$ and $\text{Li}_4\text{Cr}(\text{V})_2\text{C-II}$, we found that the former is more stable than the latter for both $\text{Li}_4\text{Cr}_2\text{C}$ and $\text{Li}_4\text{V}_2\text{C}$. Interestingly, the average adsorption energies of one, two and three layers of lithium on the V_2C monolayer surface are all far greater than those of the 1H- Cr_2C monolayer, indicating a more stable system. However, this stability order is contrary to the case of adsorption of a single lithium ion on the 1H- Cr_2C and V_2C monolayer surfaces. Moreover, the stabilities and reversible deformation of the 1H- Cr_2C and V_2C

monolayers during repeated lithiation and delithiation were investigated using the method proposed by Tritsaris, in which all lithium atoms were removed and the structure was re-optimized.⁴⁸ These calculations show that after removing all lithium atoms, the structures of the 1H- Cr_2C and V_2C monolayers are not destroyed, and they can be restored to their initial structures. All the calculated results for $\text{Li}_6\text{Cr}_2\text{C}$ and $\text{Li}_6\text{V}_2\text{C}$ meet the above four conditions of the full lithium storage phase; therefore, the maximum lithium storage concentration on the 1H- Cr_2C and V_2C monolayers correspond to $\text{Li}_6\text{Cr}_2\text{C}$ and $\text{Li}_6\text{V}_2\text{C}$, with outstanding theoretical specific capacities of 1386 and 1412 mA h g⁻¹, respectively.

The importance of strain considered in this work is mainly due to the bond length and volume change during lithiation/delithiation processes. To further evaluate the bond length and volume changes induced by lithiation/delithiation, the lengths of the Cr(V)-C bonds and the lattice constants in the xy plane of the lithiated MXenes were compared. It was found that the lengths of the Cr-C bonds slightly increase from 1.975 (Cr_2C), 1.992 ($\text{Li}_2\text{Cr}_2\text{C}$), and 1.999 ($\text{Li}_4\text{Cr}_2\text{C-I}$) to 2.006 Å ($\text{Li}_4\text{Cr}_2\text{C}$), and the lengths of the V-C bonds slightly increase from 2.049 (V_2C), 2.064 ($\text{Li}_2\text{V}_2\text{C}$), and 2.066 ($\text{Li}_4\text{V}_2\text{C-I}$) to 2.069 Å ($\text{Li}_4\text{V}_2\text{C}$) during the entire lithiation process. Additionally, the lattice constants increase slightly, from 2.659 to 2.772 Å and from 2.775 to 2.876 Å, respectively, for the 1H- Cr_2C and V_2C monolayers (about 4.2% and 3.6% tensile strain). These results indicate that the lithiation/delithiation processes can induce only small volume changes in the 1H- Cr_2C and V_2C monolayers, providing further evidence of the stability of the 1H- Cr_2C and V_2C monolayers for practical applications in LIBs.

3.4 Li diffusion on hexagonal Cr_2C and V_2C monolayers

In addition to high specific capacity, good rate capability is another requirement for a promising anode material for LIBs, especially in high power density applications such as electric

vehicles. It is known that rate capability is mainly dependent on the transport properties of lithium ions and electrons, corresponding to the lithium diffusion barriers and electronic conductivities of the 1H-Cr₂C and V₂C monolayers. In this work, LST/QST combined with the conjugate gradient (CG) refinement method was adopted to calculate the energy barriers of the transition states (TS) and intermediates for Li ion migration.⁴⁹ Considering the symmetry of the lithium favorable adsorption sites (S1 sites) on the 1H-Cr₂C and V₂C monolayer surfaces, four main diffusion pathways were considered, as depicted in Fig. 7a-d, respectively: (a) path A: lithium migration between two adjacent S1 sites through the S3 site; (b) path B: straight lithium migration between two adjacent S1 sites through the S4 site; (c) path C: lithium migration between two adjacent S1 sites through the S2 site; and (d) path D: lithium migration between two adjacent S1 sites across the honeycomb lattice along the Z direction.

The corresponding energy profiles of lithium diffusion along these four pathways on or across the 1H-Cr₂C and V₂C

monolayer surfaces are depicted in Fig. 7e and f. The calculated results reveal that for both the 1H-Cr₂C and V₂C monolayers, lithium migration by path C has the lowest activation energy barriers of 32 and 28 meV, respectively, corresponding to two transition states located near the S2 adsorption site. This ultra-low diffusion barrier is due to the smaller difference in lithium adsorption energies between the S1 and S2 adsorption sites, indicating that the lithium ions can diffuse extremely readily along this pathway. Larger diffusion energy barriers of 143 and 85 meV for lithium hopping by path A were found for the 1H-Cr₂C and V₂C monolayers, respectively, corresponding to a transition state located on the top site of the Cr(V) atom (S2 site). When lithium migrates straight between two adjacent S1 sites along path B through the S4 site, it must overcome energy barriers of 56 and 48 meV, respectively, for the 1H-Cr₂C and V₂C monolayers; this falls between path A and path C. The diffusion abilities of these three pathways on the surface planes of both the 1H-Cr₂C and V₂C monolayers were found to be path C > path B > path A, which is different from the case of

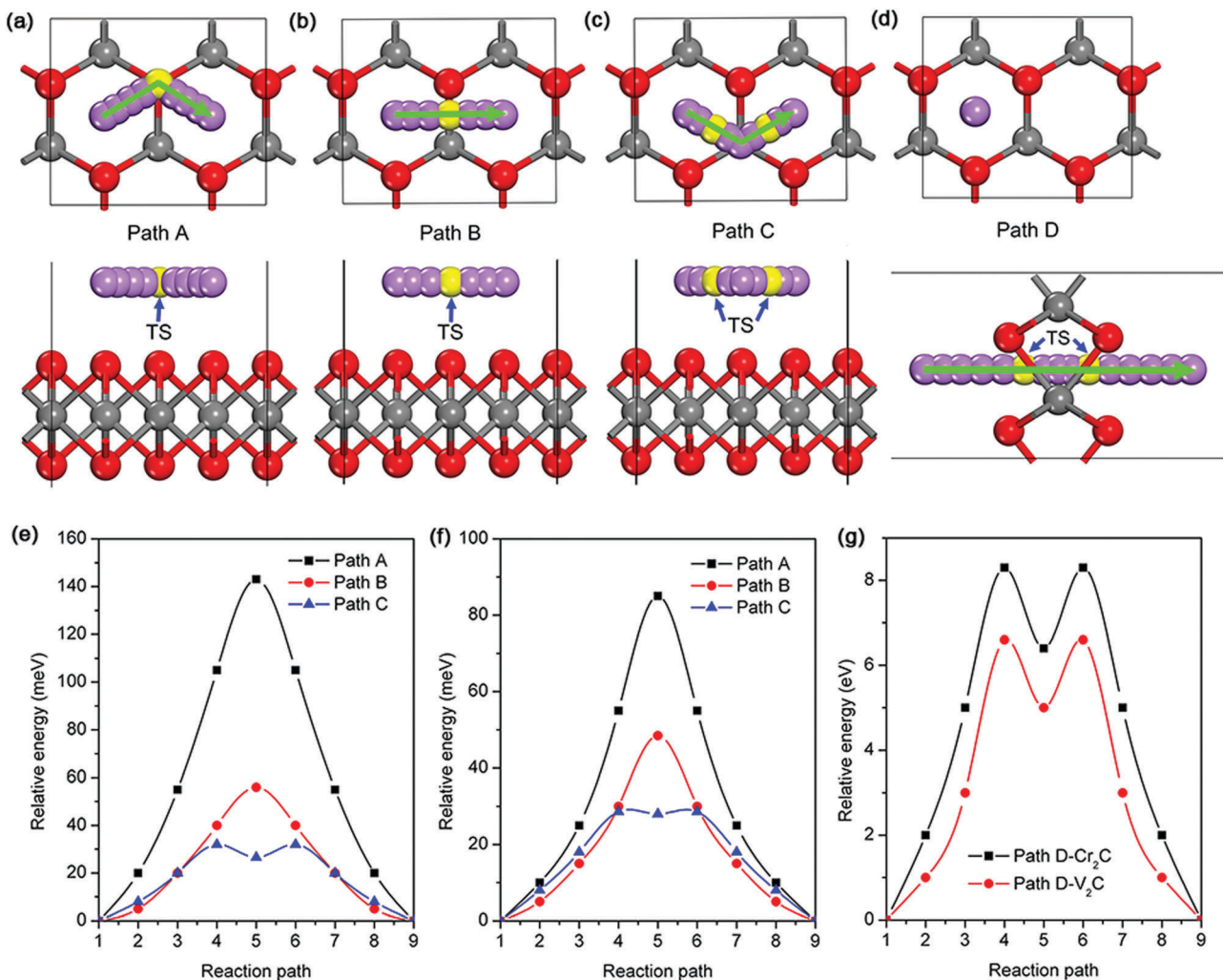


Fig. 7 Top and side views of four lithium diffusion paths: (a–c) in the plane and (d) across the plane of the 1H-Cr₂C and V₂C monolayers (here, the yellow ball site represents the transient state (TS)). Energy profiles of the corresponding lithium diffusion paths in the planes of the (e) 1H-Cr₂C and (f) 1H-V₂C monolayers (in meV); (g) energy profiles of lithium diffusion across the hexagonal hollows of the 1H-Cr₂C and V₂C monolayers (in eV).

Li diffusion on 1-H Mo₂C but similar to Na diffusion on 1-H Mo₂C.¹⁰ Moreover, for both the 1H-Cr₂C and V₂C monolayers, lithium ion migration by path D between two adjacent S1 sites across the honeycomb lattice is thermodynamically prohibited due to the extremely high energy barriers of 8.3 and 6.6 eV, respectively. Therefore, on both the 1H-Cr₂C and V₂C monolayer surfaces, the migration of lithium ions occurs on the plane. All the energy barriers of lithium migration on the V₂C monolayer are smaller than on the 1H-Cr₂C monolayer, which indicates that Li ions diffuse more readily on the V₂C monolayer. The obtained low barriers for both the 1H-Cr₂C and V₂C monolayers are comparable to other anode materials, indicating fast charge-discharge capabilities for Li.

To verify the accuracy of our energy barrier calculations using the LST/QST method, other diffusion paths starting from the TS and moving down toward the minima along both the reactant and product directions were calculated. As expected, no energy minima were found on those paths other than those of the reactant and product. It is worth noting that our lithium

diffusion barrier calculations were based on 0 K results; however, thermal vibrations in the lithiated-Cr₂C and V₂C monolayer systems are not ignorable under the actual working conditions of LIBs.

3.5 Electronic structures of the lithiated hexagonal Cr₂C and V₂C monolayers

Electronic transport is another important factor that determines the rate capability of the anode materials in LIBs; therefore, the electronic structures of the lithiated 1H-Cr₂C and V₂C monolayers were investigated by performing density of states (DOS) calculations with spin polarization, as presented in Fig. 8. In contrast to many other well-known 2D materials, which show semiconducting natures,^{15,17,18,24,50,51} the lithiated 1H-Cr₂C and V₂C monolayers are intrinsically metallic, with a large number of electronic state around the Fermi level; this is similar to some published studies.^{30,32,52,53} Thus, we can be confident that the electronic conductivities of the 1H-Cr₂C and V₂C monolayers are sufficient for their use as anode materials in LIBs with no further

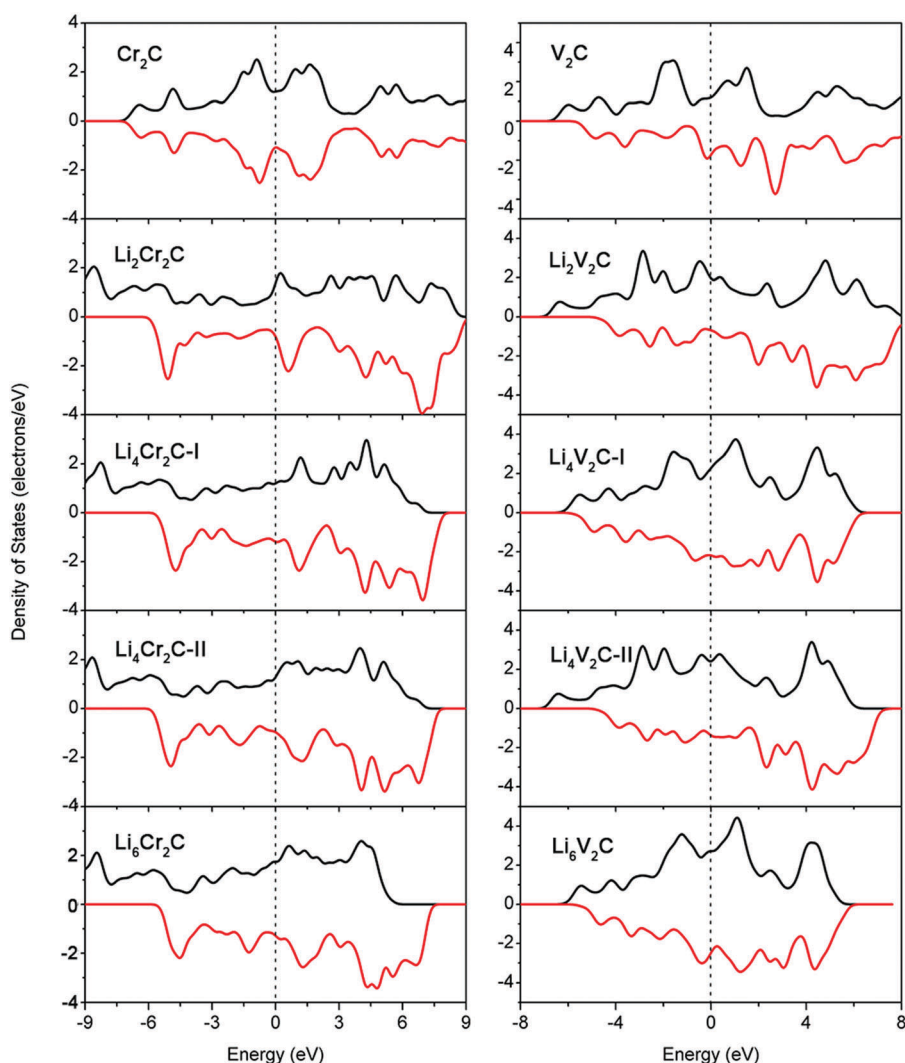


Fig. 8 Spin-polarized densities of states (DOS) of the pristine and lithiated 1H-Cr₂C and V₂C monolayer systems with different lithium concentrations. The Fermi levels were shifted to zero.

Table 3 Summary of theoretical specific capacities (mA h g^{-1}) and diffusion barriers (meV) of some currently widely investigated and promising anode materials for lithium-ion batteries

Compound	Theoretical specific capacity	Diffusion barrier	Electronic conductivity	Ref.
1H-Cr ₂ C	1386	32	Metallic	This work
1H-V ₂ C	1412	28	Metallic	This work
1H-MoS ₂	600	210	Semiconducting	54 and 55
1T-Ti ₃ C ₂	448	70	Metallic	30
1T-Ti ₂ C	166	20	Metallic	29
1T-Cr ₂ C	924		Metallic	34
1T-V ₂ C	940	45	Metallic	32
1H-Mo ₂ C	526	35	Metallic	10
Graphite	372	450–1200	Metallic	56–58
Graphyne	744	350–520	Semiconducting	59
Phosphorene	433	80	Semiconducting	17 and 50
Silicene	957	230–600	Semiconducting	48
Sn	994	390	Metallic	60
Silicon	4200	580	Semiconducting	61
Li ₄ Ti ₅ O ₁₂	175	300	Poor	62–64

structural modifications. The DOS of these structures during the lithiation and delithiation process were also calculated because the introduced lithium atoms can influence the electronic structure of the pristine phase. As the lithium concentration increases during the lithiation process, the electronic structures undergo obvious changes as a consequence of the transfer of electrons from lithium to the 1H-Cr₂C and V₂C monolayer substrates. For the lithiated-Cr₂C monolayer, the spin-up and spin-down DOS are inconsistent with each other, which shows the magnetic characteristics of lithiated Cr₂C. Also, this case is completely different from the pristine Cr₂C monolayer, indicating that the Li adatom can change the magnetism of the Cr₂C monolayer system. For the lithiated-V₂C monolayer, the spin-up and spin-down DOS are also inconsistent with each other, as in the case of the pristine V₂C monolayer. Moreover, the work functions of these lithiated hexagonal Cr₂C and V₂C monolayers were calculated; the work function determines the ease of electronic transport on the electrode surface and the electrode potential. It can be found from Table 2 that upon lithiation, the work functions of the lithiated-MXenes systems gradually decrease and are all smaller than those of the pristine MXenes, demonstrating increasing electronic transport. Not only are the metallic characteristics of the lithiated 1H-Cr₂C and V₂C nanostructures maintained, but their electronic conductivity also increases during the continual lithiation process.

3.6 Comparison with other anode materials

For a more comprehensive evaluation of the 1H-Cr₂C and V₂C monolayer materials, the theoretical specific capacities, diffusion barriers and electronic conductivities of some other currently widely investigated anode materials for lithium-ion batteries from references are summarized in Table 3. It can be seen that the 1H-V₂C and Cr₂C monolayers have the second and third largest theoretical specific capacities, the second lowest diffusion barriers and the best electronic conductivities among all the listed anode materials. Although the theoretical specific capacities of lithium storage on the 1H-Cr₂C and V₂C monolayers are about 3 times lower than that of silicon anode, their electronic

and ionic conductivities are much faster than those of silicon, which has semiconducting characteristics and a larger energy barrier, indicating that the 1H-Cr₂C and V₂C monolayers have much better rate capability. Compared to other 2D materials with semiconducting characteristics, the specific capacities of the 1H-Cr₂C and V₂C monolayers are almost 2 times that of graphyne and almost 3 times those of phosphorene and MoS₂. In addition, the lithium ion diffusion and electronic conductivities of the 1H-Cr₂C and V₂C monolayers are estimated to be faster than those of graphyne, phosphorene and MoS₂ at room temperature. Our 1H-Cr₂C and V₂C monolayers are comparable to other 2D MXene materials with high electronic conductivities. Making comparison between 1H-Cr₂C and V₂C monolayers, we found that all the calculated properties of the 1H-V₂C monolayer, including the thermal and dynamical stability, theoretical specific capacity and ionic conductivity, are superior to those of the 1H-Cr₂C monolayer; thus, 1H-V₂C is the outstanding material of the two. All this evidence demonstrates that both the 1H-Cr₂C and V₂C monolayers are promising candidates, with high capacities and high rate capabilities, for anode materials in lithium-ion batteries.

4. Conclusion

In this work, first-principles calculations based on DFT and AIMD simulations were performed to explore the potential of hexagonal Cr₂C and V₂C monolayers as anode materials in LIBs. Based on the AIMD simulations and phonon dispersion curves, the honeycomb structure of the hexagonal Cr₂C and V₂C monolayers is thermodynamically and dynamically stable. A single lithium atom is preferentially adsorbed over the center of the honeycomb lattice, with large adsorption energies of -0.463 and -0.451 eV, respectively, for hexagonal Cr₂C and V₂C monolayers. The adsorption energies per lithium atom gradually decrease as the number of lithium layers increases due to enhanced Li-Li electrostatic repulsion. Moreover, the full lithium storage phases of the hexagonal Cr₂C and V₂C monolayers correspond to Li₆Cr₂C and Li₆V₂C, with theoretical specific capacities of 1386 and 1412 mA h g^{-1} , respectively, which is much larger than those of other 2D materials. Interestingly, lithium ion diffusion on the hexagonal Cr₂C and V₂C monolayers is extremely fast, with low energy barriers of 32 and 28 meV, respectively; this is much lower than those of other widely investigated anode materials. Meanwhile, the lithiated hexagonal Cr₂C and V₂C monolayers show enhanced metallic characteristics and excellent electronic conductivity during the entire lithiation process, which is superior to other widely investigated anode materials with semiconducting characteristics. Considering these excellent characteristics, it is expected that both the hexagonal Cr₂C and V₂C monolayers are promising candidates, with high capacities and high rate capabilities, for anode materials in lithium-ion batteries. We also believe that the hexagonal Cr₂C and V₂C monolayers would be outstanding anode materials for other metal-ion (e.g., Na-ion, K-ion, Mg-ion, Ca-ion and Al-ion) batteries and that the computational method used here is transplantable.

Acknowledgements

We sincerely acknowledge the High Performance Computing Center of CSU, China. This work was financially supported by the National Natural Science Foundation of China (No. 51674302).

References

- 1 L. Wu, W. H. Lee and J. Zhang, *Mater. Today*, 2014, **1**, 82–93.
- 2 T. A. Baker, C. M. Friend and E. Kaxiras, *J. Chem. Phys.*, 2008, **129**, 104702.
- 3 S. P. Ong, V. L. Chevrier and G. Ceder, *Phys. Rev. B: Condens. Matter Mater. Phys.*, 2011, **83**.
- 4 C. Ouyang, S. Shi, Z. Wang, X. Huang and L. Chen, *Phys. Rev. B: Condens. Matter Mater. Phys.*, 2004, **69**.
- 5 J. Jiang, C. Ouyang, H. Li, Z. Wang, X. Huang and L. Chen, *Solid State Commun.*, 2007, **143**, 144–148.
- 6 S. N. Li, J. B. Liu and B. X. Liu, *J. Power Sources*, 2016, **320**, 322–331.
- 7 C. Liu, Z. G. Neale and G. Cao, *Mater. Today*, 2016, **19**, 109–123.
- 8 P. Rozier and J. M. Tarascon, *J. Electrochem. Soc.*, 2015, **162**, A2490–A2499.
- 9 J. B. Goodenough, *Energy Storage Mater.*, 2015, **1**, 158–161.
- 10 Y. D. Qilong Sun, Y. Ma, T. Jing, W. Wei and B. Huang, *J. Phys. Chem. Lett.*, 2016, **7**, 931–943.
- 11 X. Zhou, Z. Wang, W. Chen, L. Ma, D. Chen and J. Y. Lee, *J. Power Sources*, 2014, **251**, 264–268.
- 12 Y. Liu, Y. Zhao, L. Jiao and J. Chen, *J. Mater. Chem. A*, 2014, **2**, 13109.
- 13 Y. Zhu, S. Murali, W. Cai, X. Li, J. W. Suk, J. R. Potts and R. S. Ruoff, *Adv. Mater.*, 2010, **22**, 3906–3924.
- 14 Z. Xu, X. Lv, J. Li, J. Chen and Q. Liu, *RSC Adv.*, 2016, **6**, 25594–25600.
- 15 Y. Li, L. Xu, H. Liu and Y. Li, *Chem. Soc. Rev.*, 2014, **43**, 2572–2586.
- 16 A. L. Ivanovskii, *Prog. Solid State Chem.*, 2013, **41**, 1–19.
- 17 W. Li, Y. Yang, G. Zhang and Y. W. Zhang, *Nano Lett.*, 2015, **15**, 1691–1697.
- 18 G. C. Guo, X.-L. Wei, D. Wang, Y. Luo and L.-M. Liu, *J. Mater. Chem. A*, 2015, **3**, 11246–11252.
- 19 Y. Cai, Q. Ke, G. Zhang, Y. P. Feng, V. B. Shenoy and Y.-W. Zhang, *Adv. Funct. Mater.*, 2015, **25**, 2230–2236.
- 20 J. Y. Sina Najmaei, J. Zhang, P. Ajayan and J. Lou, *Acc. Chem. Res.*, 2015, **48**, 31–40.
- 21 X. Zhou, L. J. Wan and Y. G. Guo, *Chem. Commun.*, 2013, **49**, 1838–1840.
- 22 D. Kong, H. Wang, J. J. Cha, M. Pasta, K. J. Koski, J. Yao and Y. Cui, *Nano Lett.*, 2013, **13**, 1341–1347.
- 23 C. Zhang, Z. Wang, Z. Guo and X. W. Lou, *ACS Appl. Mater. Interfaces*, 2012, **4**, 3765–3768.
- 24 Y. H. Lee, X. Q. Zhang, W. Zhang, M. T. Chang, C. T. Lin, K. D. Chang, Y. C. Yu, J. T. Wang, C. S. Chang, L. J. Li and T. W. Lin, *Adv. Mater.*, 2012, **24**, 2320–2325.
- 25 C. Xu, L. Wang, Z. Liu, L. Chen, J. Guo, N. Kang, X. L. Ma, H. M. Cheng and W. Ren, *Nat. Mater.*, 2015, **14**, 1135–1141.
- 26 H. J. Zhang, K. X. Wang, X. Y. Wu, Y. M. Jiang, Y. B. Zhai, C. Wang, X. Wei and J. S. Chen, *Adv. Funct. Mater.*, 2014, **24**, 3399–3404.
- 27 M. Naguib, J. Come, B. Dyatkin, V. Presser, P. L. Taberna, P. Simon, M. W. Barsoum and Y. Gogotsi, *Electrochem. Commun.*, 2012, **16**, 61–64.
- 28 M. Naguib, J. Halim, J. Lu, K. M. Cook, L. Hultman, Y. Gogotsi and M. W. Barsoum, *J. Am. Chem. Soc.*, 2013, **135**, 15966–15969.
- 29 S. Zhao, W. Kang and J. Xue, *J. Phys. Chem. C*, 2014, **118**, 14983–14990.
- 30 D. Er, J. Li, M. Naguib, Y. Gogotsi and V. B. Shenoy, *ACS Appl. Mater. Interfaces*, 2014, **6**, 11173–11179.
- 31 Y. Xie, M. Naguib, V. N. Mochalin, M. W. Barsoum, Y. Gogotsi, X. Yu, K. W. Nam, X. Q. Yang, A. I. Kolesnikov and P. R. Kent, *J. Am. Chem. Soc.*, 2014, **136**, 6385–6394.
- 32 J. Hu, B. Xu, C. Ouyang, S. A. Yang and Y. Yao, *J. Phys. Chem. C*, 2014, **118**, 24274–24281.
- 33 C. Si, J. Zhou and Z. Sun, *ACS Appl. Mater. Interfaces*, 2015, **7**, 17510–17515.
- 34 D. Sun, Q. Hu, J. Chen, X. Zhang, L. Wang, Q. Wu and A. Zhou, *ACS Appl. Mater. Interfaces*, 2016, **8**, 74–81.
- 35 J. P. Perdew, A. Ruzsinszky and G. I. Csonka, *Phys. Rev. Lett.*, 2008, **100**, 136406.
- 36 R. C. Kari Laasonen, C. Lee and D. Vanderbilt, *Phys. Rev. B: Condens. Matter Mater. Phys.*, 1991, **43**, 6796.
- 37 H. J. Monkhorst and J. D. Pack, *Phys. Rev. B: Solid State*, 1976, **13**, 5188.
- 38 Q. Meng, T. Wang, E. Liu, X. Ma, Q. Ge and J. Gong, *Phys. Chem. Chem. Phys.*, 2013, **15**, 9549–9561.
- 39 U. Yorulmaz, A. Ozden, N. K. Perkgoz, F. Ay and C. Sevik, *Nanotechnology*, 2016, **27**, 335702.
- 40 L. F. Huang and Z. Zeng, *J. Phys. Chem. C*, 2015, **119**, 18779–18789.
- 41 L. J. Zhou, Z. F. Hou and L. M. Wu, *J. Phys. Chem. C*, 2012, **116**, 21780–21787.
- 42 L. J. Zhou, Z. F. Hou, L. M. Wu and Y. F. Zhang, *J. Phys. Chem. C*, 2014, **118**, 28055–28062.
- 43 H. N. Kunihiro Nobuhara, M. Nose, S. Nakanishi and H. Iba, *J. Power Sources*, 2013, **243**, 585–587.
- 44 Z. Xu, X. Lv, J. Li, J. Chen and Q. Liu, *Appl. Surf. Sci.*, 2016, **376**, 97–104.
- 45 Y. Xie, Y. Dall'Agnese, M. Naguib, Y. Gogotsi, M. W. Barsoum, H. L. Zhuang and P. R. C. Kent, *ACS Nano*, 2014, **8**, 9606–9615.
- 46 A. R. Mohammad Khazaei, M. Ghorbani-Asl, M. Arai, T. Sasak, Y. Liang and S. Yunoki, *Phys. Rev. B: Condens. Matter Mater. Phys.*, 2016, **93**, 205125.
- 47 Q. F. Li, C. G. Duan, X. G. Wan and J. L. Kuo, *J. Phys. Chem. C*, 2015, **119**, 8662–8670.
- 48 G. A. Tritsaris, E. Kaxiras, S. Meng and E. Wang, *Nano Lett.*, 2013, **13**, 2258–2263.
- 49 N. Govind, M. Petersen, G. Fitzgerald, D. King-Smith and J. Andzelm, *Comput. Mater. Sci.*, 2003, **28**, 250–258.

- 50 R. Zhang, X. Wu and J. Yang, *Nanoscale*, 2016, **8**, 4001–4006.
- 51 T. Komesu, D. Le, X. Zhang, Q. Ma, E. F. Schwier, Y. Kojima, M. Zheng, H. Iwasawa, K. Shimada, M. Taniguchi, L. Bartels, T. S. Rahman and P. A. Dowben, *Appl. Phys. Lett.*, 2014, **105**, 241602.
- 52 L. Chuan Xu, Z. Liu, L. Chen, J. Guo, N. Kang, X.-L. Ma, H.-M. Cheng and W. Ren, *Nat. Mater.*, 2015, **14**, 1135–1141.
- 53 J. Luo, X. Tao, J. Zhang, Y. Xia, H. Huang, L. Zhang, Y. Gan, C. Liang and W. Zhang, *ACS Nano*, 2016, **10**, 2491–2499.
- 54 J. H. Xiaobo Chen, D. Srivastava and J. Li, *Appl. Phys. Lett.*, 2012, **100**, 263901.
- 55 D. W. Yafei Li, Z. Zhou, C. R. Cabrera and Z. Chen, *J. Phys. Chem. Lett.*, 2012, **3**, 2221–2227.
- 56 M. M. I. Sascha Thinius, P. Heijmans and T. Bredow, *J. Phys. Chem. C*, 2014, **118**, 2273–2280.
- 57 R. T. Yazami and P. A. Reversible, *J. Power Sources*, 1983, **9**, 365–371.
- 58 R. A. Jishi and M. S. Dresselhaus, *Phys. Rev. B: Condens. Matter Mater. Phys.*, 1992, **45**, 12465–12469.
- 59 H. Zhang, Y. Xia, H. Bu, X. Wang, M. Zhang, Y. Luo and M. Zhao, *J. Appl. Phys.*, 2013, **113**, 044309.
- 60 J. Xiao, D. Choi, L. Cosimescu, P. Koech, J. Liu and J. P. Lemmon, *Chem. Mater.*, 2010, **22**, 4522–4524.
- 61 W. Wan, Q. Zhang, Y. Cui and E. Wang, *J. Phys.: Condens. Matter*, 2010, **22**, 415501.
- 62 T. F. Yi, Y. Xie, Y. R. Zhu, R. S. Zhu and H. Shen, *J. Power Sources*, 2013, **222**, 448–454.
- 63 B. Zhao, R. Ran, M. Liu and Z. Shao, *Mater. Sci. Eng., R*, 2015, **98**, 1–71.
- 64 W. J. Zhang, *J. Power Sources*, 2011, **196**, 13–24.